The effects of plasma electrolytically oxidized layers containing Sr and Ca on the osteogenic behavior of selective laser melted Ti6Al4V porous implants

van Hengel, I. A.J.; Laçin, M.; Minneboo, M.; Fratila-Apachitei, L. E.; Apachitei, I.; Zadpoor, A. A.

DOI
10.1016/j.msec.2021.112074

Publication date
2021

Document Version
Final published version

Published in
Materials Science and Engineering C

Materials Science & Engineering C 124 (2021) 112074

Contents lists available at ScienceDirect

Materials Science & Engineering C

journal homepage: www.elsevier.com/locate/msec

The effects of plasma electrolytically oxidized layers containing Sr and Ca on the osteogenic behavior of selective laser melted Ti6Al4V porous implants

I.A.J. van Hengel *, M. Laçin, M. Minneboo, L.E. Fratila-Apachitei, I. Apachitei, A.A. Zadpoor

Additive Manufacturing Laboratory, Department of Biomechanical Engineering, Faculty of Mechanical, Maritime, and Materials Engineering, Delft University of Technology, the Netherlands

ARTICLE INFO

Keywords:
Plasma electrolytic oxidation
Additive manufacturing
Strontium
Oxidation time
Current density
Surface biofunctionalization
Titanium bone implants

ABSTRACT

Surface biofunctionalization is frequently applied to enhance the functionality and longevity of orthopedic implants. Here, we investigated the osteogenic effects of additively manufactured porous Ti6Al4V implants whose surfaces were biofunctionalized using plasma electrolytic oxidation (PEO) in Ca/P-based electrolytes with or without strontium. Various levels of Sr and Ca were incorporated in the oxide layers by using different current densities and oxidation times. Increasing the current density and oxidation time resulted in thicker titanium oxide layers and enhanced the release of Ca^{2+} and Sr^{2+}. Biofunctionalization with strontium resulted in enhanced pore density, a thinner TiO_2 layer, four-fold reduced release of Ca^{2+}, and mainly anatase phases as compared to implants biofunctionalized in electrolytes containing solely Ca/P species under otherwise similar conditions. Different current densities and oxidation times significantly increased the osteogenic differentiation of MC3T3-E1 cells on implants biofunctionalized with strontium, when the PEO treatment was performed with a current density of 20 A/dm^2 for 5 and 10 min as well as for a current density of 40 A/dm^2 for 5 min. Therefore, addition of Sr in the PEO electrolyte and control of the PEO processing parameters represent a promising way to optimize the surface morphology and osteogenic activity of future porous AM implants.

1. Introduction

The demand for orthopedic bone implants that last for extensive lifetimes is increasing [1]. To support the longevity of cementless bone implants, proper fixation between implant and bone tissue is of utmost importance. Such implants are increasingly made using additive manufacturing (AM), as it allows for the free-form fabrication of customized (titanium) implants for a variety of purposes including the treatment of large bony defects [2–4]. The mechanical behavior of AM porous implants can be controlled through geometrical design to further enhance the longevity of such implants [5,6]. The highly porous nature of such implants means that they possess vast surface areas, which make these implants prone to infection. Surface biofunctionalization of these AM implants has been, therefore, used to not only prevent implant-associated infections but also to stimulate osteogenic properties [7] of AM porous implants. Such biofunctionalization procedures, however, have been found to be challenging.

Plasma electrolytic oxidation (PEO) is an electrochemical surface treatment that has been shown to enhance the bioactivity of titanium implants [8–10]. PEO transforms the native amorphous titanium oxide surface layer into a surface consisting of nanocrystalline titanium oxide phases in a single-step process [11,12]. At the start of the PEO process, the voltage rises steadily until dielectric breakdown occurs, resulting in local spark discharges at the interface between substrate and electrolyte [13]. As the surface layer grows, the spark discharges decrease in number, but increase in intensity. With increasing oxidation time, gas bubbles arise at the surface contributing to the development of large, protruding pores. At the same time, nanocrystalline phases form as a result of the locally high temperatures that are experienced during the spark discharges and the accompanying pressures. During layer growth, species from the electrolytes as well as from the titanium substrates are incorporated in the porous oxide layer.

PEO is suitable for the surface biofunctionalization of complex, porous geometries [14], does not alter the mechanical behavior of the substrate due to limited heat input [15], and results in strong bonding between the titanium oxide layer and the substrate [16–19]. The

* Corresponding author.
E-mail address: i.a.j.vanhengel@tudelft.nl (I.A.J. van Hengel).

https://doi.org/10.1016/j.msec.2021.112074
Received 14 August 2020; Received in revised form 26 February 2021; Accepted 7 March 2021
Available online 31 March 2021

bioactivity of the implant surface can be adjusted through the composition of the PEO electrolyte. The use of Ca/P-based electrolytes results in the formation of crystalline Ca/P phases including hydroxyapatite [20–22], which can stimulate bone tissue regeneration. Through the addition of inorganic nanoparticles, such as Ag, Cu, and/or Zn, the implant surfaces are endowed with antibacterial properties [23,24].

Strontium has been used to treat osteoporotic patients effectively due to its initiation of bone formation and its simultaneous reduction of bone resorption, thereby reducing the risk of fracture [25,26]. However, systemic strontium intake may induce cardiac events [27]. Therefore, local administration at low, yet effective doses, is necessary to prevent the side effects associated with the medicinal use of strontium [28]. As such, strontium has been applied on the surface of titanium biomaterials and has been shown to enhance the osteogenic differentiation of mesenchymal stromal cells *in vitro* [29,30] and repair bone defects *in vivo* [31,32]. Titanium biomaterials treated with strontium using PEO have been shown to result in enhanced osteogenic properties [33–35].

Apart from altering the chemical composition of the PEO electrolyte, the electrical processing parameters can change the surface morphology of the implants and the phase composition. For example, increasing the current density and oxidation time will result in thicker oxide layers, larger surface pores and increased formation of crystalline phases [36,37].

The contributions of these processing parameters to the osteogenic properties of the resulting surfaces have not yet been investigated. The characterization of the surface morphology and osteogenic properties is required to understand the missing link between the surface biofunctionalization process and the resulting bioactivity. Insight into these effects will contribute to an optimized performance of future orthopedic implants. In previous research [38], we have observed a synergistic effect of the incorporated Sr and Ag on the antibacterial activity of PEO-treated porous AM titanium implants highlighting the potential of further optimization of the incorporated elements for achieving the desired biofunctionalities. Therefore, in this study, we incorporated different levels of Sr into the titanium implants by modifying the PEO processing parameters including the current density and oxidation time, and assessed their effects on the surface morphology and the osteogenic properties of porous AM titanium implants.

2. Materials and methods

2.1. Implant manufacturing and surface biofunctionalization

Porous Ti-6Al-4 V implants were rationally designed and manufactured by AM as previously described [14]. Biofunctionalization of these implants was performed by PEO using a customized setup which included an AC power source (ACS 1500, 50 Hz, ET power Systems Ltd., Chesterfield, United Kingdom), connected to a data acquisition board through a computer interface (SCXI, National Instruments, Austin, Texas, United States), and an electrolytic cell consisting of double-walled glass. During PEO processing, the implant functioned as the anode while a stainless steel cylinder formed the cathode. The PEO electrolyte was continuously stirred at 500 rpm and voltage-time (V-t) transients were sampled at a rate of 1 Hz.

The PEO electrolyte was prepared by dissolving 0.15 M calcium acetate (Sigma-Aldrich, St. Louis, Missouri, United States) and 0.02 M calcium glycerophosphate (Dr. Paul Lohmann GmbH, Emmerthal, Germany) in 800 ml demineralized water supplemented with 1.0 M strontium acetate (Sigma-Aldrich). The conductivity of the electrolytes was measured in three-fold using a conductivity meter (Consort, Topac Inc., Cohasset, Massachusetts, United States). The experimental groups included implants without any PEO biofunctionalization and were labelled non-treated (NT), implants that were treated with PEO but without strontium acetate (PT), and PEO-treated implants with strontium acetate (PT – Sr). The PEO processing was conducted galvanostatically using RMS current densities of 20, 30, and 40 A/dm^2 for 5 and 10 min with sinusoidal input signals. After PEO biofunctionalization, the implants were rinsed under running tap water for 1 min, sonicated in 70% ethanol for 30 s, rinsed in demineralized water for 5 min, sonicated in demineralized water for 30 s and sterilized in an oven at 110 °C for 1 h.

2.2. Assessment of titanium oxide layer and surface morphology

In order to investigate the titanium oxide layer surrounding the implant, cross-sections were prepared (n = 3/group). Therefore, perpendicular sections were made along the longitudinal axis of the implant and fixed in a conductive resin (Polyfast, Struers, Copenhagen, Denmark). Then, the specimens were successively ground for 2 min each with 80, 180, 320, 800, 1200, 2000 and 4000 *SiC* abrasive paper successively (Struers, Copenhagen, Denmark) using tap water for lubrication. The grinding steps were followed by ultrasonication in isopropanol for 5 min and air drying. Finally, the specimens were polished with DiaDuo-2 suspension (Struers) containing diamonds of 3 μm, rinsed with isopropanol and tap water, and then polished with DiaDuo-2 diamonds of 1 μm.

To characterize the morphology of the implant surfaces, scanning electron microscopy (SEM, JSM-IT100LV, JEOL, Tokyo, Japan) was used. In order to increase the electrical conductivity, a gold layer of 5 ± 2 nm was sputtered onto the surface. SEM imaging was performed at a working distance of 10 mm and an electron beam energy between 5 and 20 kV. The thickness and porosity were measured at 5 different spots on 3 implants for each experimental group. Pore diameter and pore density were determined using ImageJ. Chemical analysis was performed by energy-dispersive X-ray spectroscopy (EDS) at 6 different spots for each experimental group.

2.3. Inductively coupled plasma optical emission spectrometry

The ion release profiles of Ca^{2+} and Sr^{2+} were evaluated using inductively coupled plasma – optical emission spectrometry (ICP-OES). The ion release of the biofunctionalized implants (n = 3/group) was studied through the immersion of 1 cm implants in 1 ml phosphate-buffered saline (PBS) in light-shielding 1.5 ml Eppendorf tubes at 37 °C under static conditions. The PBS was sampled and refilled after ½, 1, 2, 4, 7, 15, and 30 days. Subsequently, the sampled PBS was diluted in 5% nitric acid. The chemical element levels were measured by ICP-OES (Spectro Arcos, Kleve, Germany).

2.4. X-ray diffraction

To investigate the composition of phases present on the implant surfaces, X-ray diffraction (XRD) analysis was conducted using a D8 advanced diffractometer (Bruker, Billerica, Massachusetts, United States). For XRD analysis, the following settings were used: voltage = 45 kV, current = 40 mA, scatter screen height = 5 mm, and CuKα radiation detector = LL 0.11 W 0.14. The specimens were analyzed statically with a coupled θ - 2θ scan ranging from 20 to 120°, a counting rate of 5 s/step, and a step size of 0.030° 2θ. Subsequently, the collected data was evaluated using DiffracSuite.Eva (version 5.0, Bruker).

2.5. Osteogenic cell response

2.5.1. Cell seeding and culturing

The osteogenic properties of the implant surfaces were evaluated using preosteoblast cells (MC3T3-E1, Sigma-Aldrich). We tested the osteogenic capacity of NT, PT – 20 A/dm^2–5 min, and all PT – Sr implants. The cells were pre-cultured for 7 days in α-MEM supplemented with 10% fetal bovine serum and 1% penicillin-streptomycin (both from ThermoFisher, Waltham, Massachusetts, United States). During experimentation, the cell culture medium was renewed every 2–3 days. In order to seed the cells, implants of 1.0 cm length were placed in 0.2 ml

tubes together with 100 μl culture medium containing 1.5×10^5 cells. Subsequently, the tubes were kept in an incubator (at 37 °C, 5% CO_2) and tilted every 20 min for 2 h. Thereafter, the samples were transferred into a 48 well plate with 200 μl fresh medium. We performed the experiments under two conditions: either in standard culture medium throughout the entire experiment or switching after 2 days of culture to osteogenic medium through supplementation of the standard culture medium with 50 μg/ml ascorbic acid and 4 mM β-glycerophosphate (all from Sigma-Aldrich).

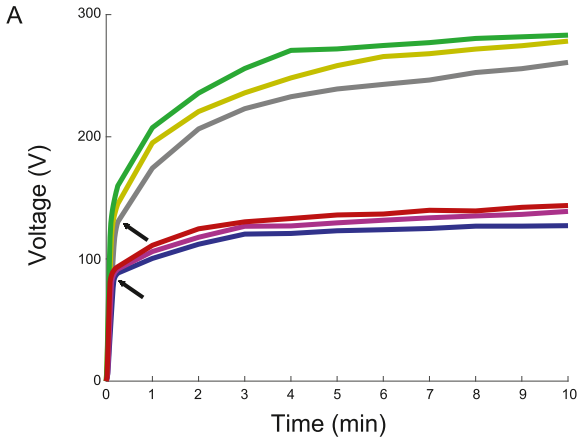

B

	Electrolyte conductivity (mS/cm)
PT	10.4 ± 0.1
PT – Sr	34.1 ± 0.1

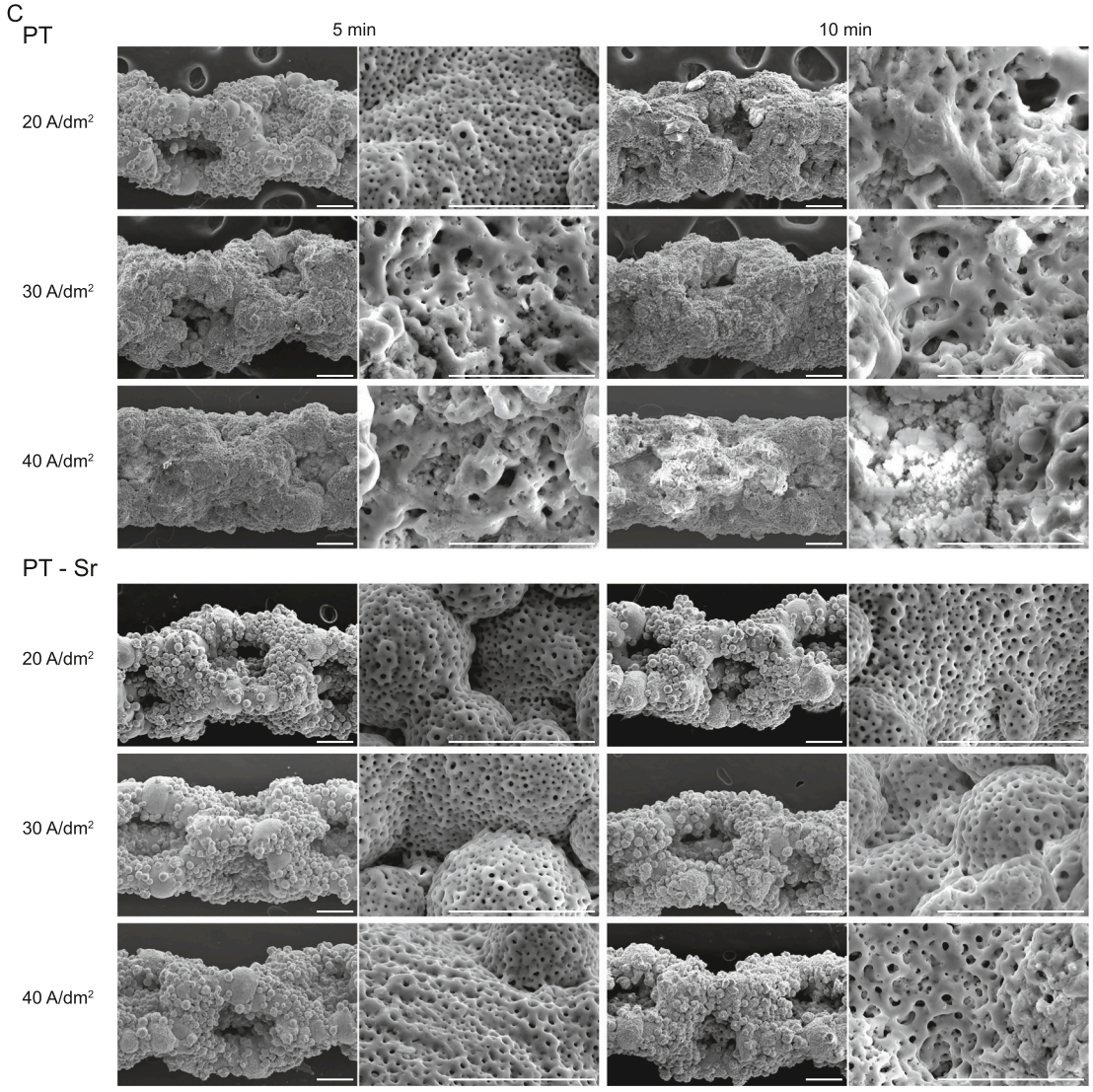

Fig. 1. (A) The V-t transients registered during the PEO processing of AM Ti-6Al-4 V implants. Arrows indicate dielectric breakdown. (B) The electrolyte conductivity of PT and PT – Sr electrolytes ($n = 3$). (C) The SEM images showing the surface morphology of the implants after PEO biofunctionalization. Scale bars are 200 μm (low magnifications) and 40 μm (high magnifications).

2.5.2. Metabolic activity assay

To determine the metabolic activities of the MC3T3-E1 cells on the implants, a Presto Blue assay (Thermofisher, Waltham, MA, United States) was performed after 1, 3, 7, 11, and 14 days. At these time points, 20 μl Presto Blue reagent and 180 μl fresh culture medium were added to the implants, which were subsequently kept in the incubator for 1 h at 37 °C. Finally, the absorbance of the supernatant was determined at 530 nm excitation wavelength and 590 nm emission wavelength using a micro-plate reader (Victor X3, PerkinElmer, Groningen, The Netherlands).

2.5.3. Alkaline phosphatase assay

Osteogenic differentiation was investigated after 11 and 14 days by measuring the alkaline phosphatase (ALP) activity of the MC3T3-E1 cells. Therefore, the specimens ($n = 4$/group) were cleansed in PBS, submerged in 250 μl of PBS-Triton (containing 0.1% Triton X-100) and subsequently the specimens were ultrasonicated for 10 min, to dissociate the cells from the implant. Then, the specimens were kept in 100 μl *p*-nitrophenyl phosphate (pNPP, Sigma-Aldrich) at 37 °C for 10 min after which 250 μl of NaOH was supplemented to halt the process. The ALP activity was determined using a standard curve with 0–100 μl of pNPP, with 100 μl of PBS-Triton as well as 250 μl of NaOH in every well. Subsequently, the absorbance measurement was performed at a wavelength of 405 nm with a Victor X3 plate reader (PerkinElmer). Finally, using a bicinchoninic acid (BCA) kit (Invitrogen, California, United States), the overall protein content of every specimen was measured, followed by the normalization of the ALP activity to the overall protein content.

2.5.4. Cell morphology

The morphology of the cells cultured on the implant surfaces was analyzed by SEM after 7 days of culture ($n = 2$/group). To that end, the specimens were fixated for 20 min in McDowels fixative consisting of 4% paraformaldehyde and 1% glutaraldehyde in 10 mM phosphate buffer at pH 7.4 and kept in demineralized water at 4 °C. Then, the specimens were rinsed two times in demineralized water for 5 min, dehydrated in diluted ethanol series of 50% for 15 min, 70% for 20 min, and 96% for 20 min, and air-dried for 2 h. Subsequently, the specimens were sputtered with a 5 ± 2 nm gold layer and investigated by SEM.

2.6. Statistical analysis

All statistical analyses were performed using GraphPad Prism (GraphPad Software, La Jolla, California, United States) applying one-way and repeated-measures ANOVA and Bonferroni *post hoc* tests. Data are reported as mean ± standard deviation. The differences between the groups were considered statistically significant at $p < 0.05$.

3. Results

3.1. Voltage transients

The recorded V-t curves demonstrated that implant biofunctionalization by PEO resulted in higher voltages for the PT implants in comparison with PT–Sr implants (Fig. 1A). Initially, the voltage rose sharply until the dielectric breakdown with a rate of 12, 15, and 18 V/s for PT–20 A/dm^2, PT–30 A/dm^2 and PT–40 A/dm^2, respectively. The dielectric breakdown occurred after 10 ± 2 s at 117 ± 2 V for PT–20 A/dm^2, after 8 ± 1 s at 119 ± 2 V for PT–30 A/dm^2, and after 7 ± 1 s at 129 ± 2 V for PT–40 A/dm^2. For the PT–Sr groups, the dielectric breakdown occurred after 8 ± 1 s at 80 ± 1 V, after 6 ± 1 s at 80 ± 3 V, and after 5 ± 1 s at 81 ± 4 V for 20 A/dm^2, 30 A/dm^2 and 40 A/dm^2, respectively. After the dielectric breakdown, the slope of the V-t curve inflected resulting in a final voltage (after 10 min of oxidation) of 261 ± 3 V, 278 ± 6 V, and 283 ± 3 V for the PT–20 A/dm^2, PT–30 A/dm^2, and PT–40 A/dm^2 groups, respectively while the voltage rose to 127 ± 2 V for PT–Sr–20 A/dm^2, 139 ± 5 V for PT–Sr–30 A/dm^2 and 144 ± 3 V for PT–Sr–40 A/dm^2. The electrical conductivity of the PT – Sr electrolyte was enhanced more than three-fold compared to that of the PT electrolyte (Fig. 1B).

3.2. Implant surface morphology after PEO biofunctionalization

Following PEO biofunctionalization, the implant surface morphology was analyzed by SEM (Fig. 1C). All conditions displayed a homogenous coverage of the titanium oxide layer over the entire implant as identified by a highly interconnected microporous surface, which is characteristic for PEO biofunctionalization. Oxidation of the PT implants for 5 min with 20 A/dm^2 resulted in the highest pore density with the smallest pore sizes while PEO biofunctionalization with increased current densities resulted in relatively rougher surfaces with fewer pores and larger pore sizes (Table 1). Enhancing the oxidation time from 5 to 10 min resulted in an even further enlargement of pore sizes and the roughening of the surface except for 10 min with 40 A/dm^2 which showed reduced pore sizes compared to 10 min with 30 A/dm^2. In the case of the PT–Sr implants, the changes in morphology were less prominent. Increasing the current density did not result in a change in the surface morphology of the implants after 5 min. After 10 min, however, the PT–Sr–30 A/dm^2 and PT–Sr–40 A/dm^2 groups revealed a less circular pore shape and the roughening of their surfaces. EDS analysis demonstrated the presence of Ti, Al, O, C, P, Ca and Sr species and indicated that Ca was largely replaced by Sr when comparing PT and PT–Sr implants (Table 1).

3.3. Cross-section morphology and thickness of the biofunctionalized TiO_2 layers

The morphology and thickness of the titanium oxide surface layers were analyzed through cross-section analysis by SEM (Fig. 2A). For the PT implants, the oxide layer morphology differed across their thickness. At the interface with the substrate (inner side), a fully dense and uniform layer with an intact interface with the substrate was observed for all the implant groups. This barrier layer had a thickness of *ca.* 2 μm. Moving outwards, a porous morphology was visible while the surface oxide layer was found to be dense in all the groups except for the PT– 10 min–40 A/

Table 1
Porosity and chemical analysis of the implant surfaces. The proportion of chemical elements is indicated as at.%.

	Pore density (%)	Pore diameter (μm)	Ca (at.%)	Sr (at.%)
PT – 5 min – 20A/dm^2	2.6 ± 0.1	2.7 ± 1.1	9.8 ± 2.9	–
PT – 5 min – 30A/dm^2	2.2 ± 0.7	3.3 ± 1.7	7.1 ± 2.0	–
PT – 5 min – 40A/dm^2	1.6 ± 0.5	5.2 ± 1.9	7.8 ± 2.2	–
PT – 10 min – 20A/dm^2	0.8 ± 0.4	4.5 ± 3.2	9.1 ± 2.5	–
PT – 10 min – 30A/dm^2	0.6 ± 0.2	4.9 ± 2.4	9.7 ± 2.9	–
PT – 10 min – 40A/dm^2	0.4 ± 0.2	2.0 ± 1.5	8.1 ± 1.4	–
PT – Sr – 5 min – 20A/dm^2	1.2 ± 0.5	1.3 ± 0.3	0.5 ± 0.1	3.0 ± 0.5
PT – Sr – 5 min – 30A/dm^2	1.2 ± 0.1	1.5 ± 0.4	0.7 ± 0.3	3.5 ± 1.4
PT – Sr – 5 min – 40A/dm^2	2.0 ± 0.4	1.7 ± 0.4	0.7 ± 0.1	3.8 ± 0.4
PT – Sr – 10 min – 20A/dm^2	1.3 ± 0.9	1.4 ± 0.3	1.8 ± 0.8	11.9 ± 5.5
PT – Sr – 10 min – 30A/dm^2	2.5 ± 0.3	2.3 ± 0.6	1.1 ± 0.3	7.2 ± 2.5
PT – Sr – 10 min – 40A/dm^2	3.6 ± 0.8	2.0 ± 0.4	1.0 ± 0.2	3.5 ± 0.6

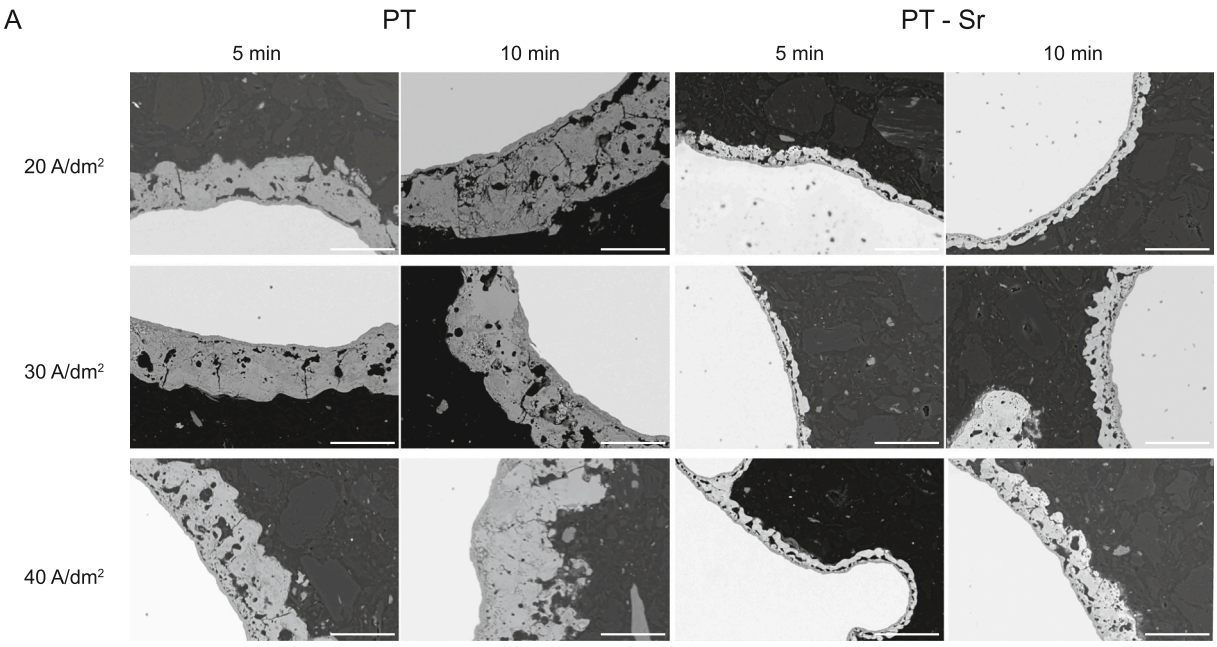

B

	Pore diameter (μm)
PT – 5min – 20A/dm²	2.7 ± 1.3
PT – 5min – 30A/dm²	4.2 ± 1.7
PT – 5min – 40A/dm²	4.3 ± 1.5
PT – 10min – 20A/dm²	3.9 ± 1.2
PT – 10min – 30A/dm²	5.1 ± 2.0
PT – 10min – 40A/dm²	4.5 ± 2.5
PT – Sr – 5min – 20A/dm²	1.8 ± 0.9
PT – Sr – 5min – 30A/dm²	2.3 ± 1.2
PT – Sr – 5min – 40A/dm²	2.5 ± 0.8
PT – Sr – 10min – 20A/dm²	2.6 ± 1.7
PT – Sr – 10min – 30A/dm²	3.1 ± 1.4
PT – Sr – 10min – 40A/dm²	3.4 ± 1.6

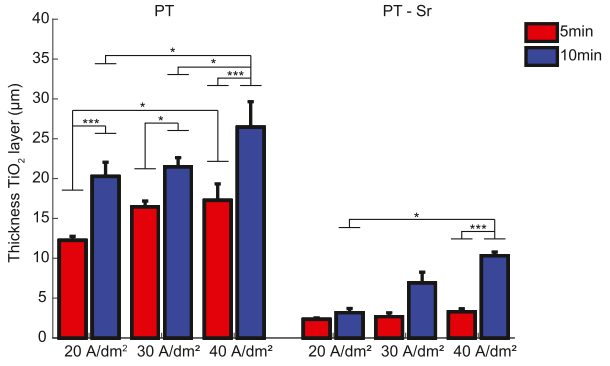

Fig. 2. The thickness of the surface layer of TiO_2 implants. (A) The SEM images of the surface layer in backscattering mode. (B) Cross-sectional pore-size analysis by SEM ($n = 3$). (C) A quantitative analysis of the thickness of the implant surface layers ($n = 3$). * $p < 0.05$, *** $p < 0.001$. Scale bar = 10 μm.

dm^2 group, which only displayed a porous outer layer. The PT–Sr implant groups also displayed a fully dense oxide layer at the implant substrate interface, followed by a middle porous layer, and a denser surface layer on top. Increasing the current density and oxidation time resulted in enhanced cross-sectional pore sizes up to an oxidation time of 10 min with 40 A/dm^2 (Fig. 2B).

The thickness of the implant oxide layer was enhanced both by an increased current density and an increased oxidation time (Fig. 2C). For the PT implants, the thickness of the oxide layer increased after 10 min as compared to 5 min for treatments with current densities of 20, 30, and 40 A/dm^2 ($p < 0.001$, $p < 0.05$ and $p < 0.001$, respectively), after 5 min with 40 A/dm^2 as compared to 20 A/dm^2 ($p < 0.05$), and after 10 min with 40 A/dm^2 as compared to 20 A/dm^2 and 30 A/dm^2 ($p < 0.05$). For the PT–Sr implants, the oxide layer was enhanced after oxidation for 10 min with 40 A/dm^2 as compared to 5 min with 40 A/dm^2 and as compared to 10 min with 20 A/dm^2 ($p < 0.001$). The thickness of the titanium oxide layer was significantly larger for the PT implants in comparison with the PT–Sr implants under similar current densities and oxidation times, varying between 12 and 26 μm for the PT implants and between 2 and 10 μm for the PT–Sr implants.

3.4. Ion release kinetics

The Ca and Sr ion release kinetics were analyzed by ICP-OES for up to 30 days. For the PT implants, the Ca^{2+} release was increased 1.37 fold for treatment with a current density of 40 A/dm^2 as compared to a current density of 30 A/dm^2 (Fig. 3A). Comparing 5 and 10 min of oxidation time resulted in 1.21, 1.28, and 1.14 fold increase in the Ca^{2+} release for the PT implants treated with current densities of 20, 30, and 40 A/dm^2, respectively. For the PT–Sr implants, the Ca^{2+} released increased by 1.26 fold for the implants treated with a current density of 40 A/dm^2 as compared to those subjected to a current density of 30 A/dm^2 while treatment with 10 min as compared to 5 min resulted in 0.97, 1.16, and 1.30 fold increase in the Ca^{2+} release for the PT–Sr implants treated with current densities of 20, 30, and 40 A/dm^2, respectively. The Ca^{2+} release was at least 4-fold higher for all the PT implants as compared to the PT–Sr implants. Furthermore, for both the PT and PT–Sr implants, the Ca^{2+} release was highest for 10 min and a current density of 40 A/dm^2.

The Sr^{2+} release was the highest for 10 min oxidation with 40 A/dm^2 and increased with both the oxidation time and current density (Fig. 3B). The Sr^{2+} release was 2.49 and 2.09 fold higher when the current density increased from 20 to 30 A/dm^2 for 5 and 10 min oxidation time, respectively. The implants treated with 40 A/dm^2 further increased the Sr^{2+} release by 1.54 fold. Elongating the oxidation time from 5 to 10 min, resulted in 2.98, 2.50, and 2.48 fold increase in the Sr^{2+} release for the PT–Sr implants treated with current densities of 20, 30, and 40 A/dm^2, respectively. The PT–Sr implants released between 0.63 and 2.11

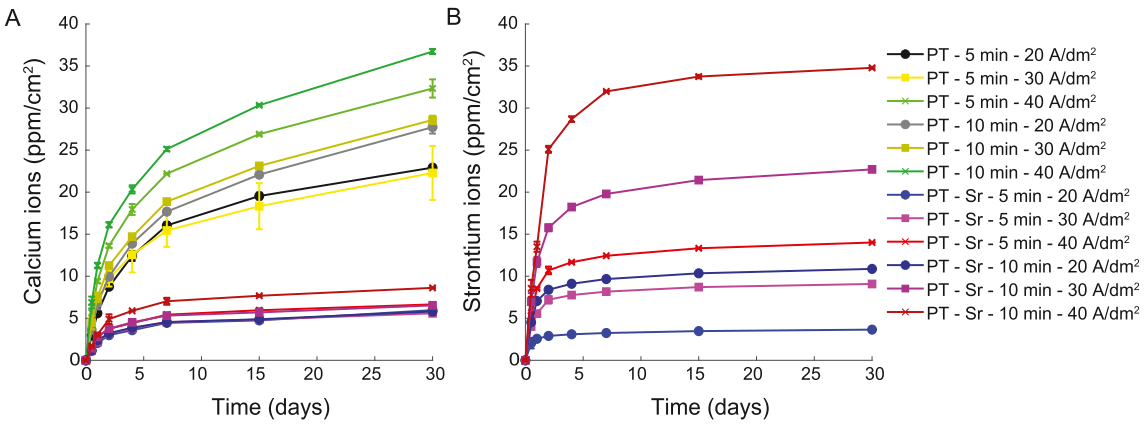

Fig. 3. The cumulative ion release profiles. (A) The calcium and (B) strontium ion release from the implant surfaces ($n = 3$) measured by ICP-OES.

fold higher levels of Sr^{2+} as compared to Ca^{2+} after 5 min and between 1.87 and 4.04 fold after 10 min.

3.5. Phase composition of the titanium oxide layer

The phase composition of the implants' oxide layer was evaluated by XRD (Fig. 4). While differences in the phase composition were frequently observed between 5 and 10 min of oxidation time, few phase changes were observed between the current densities of 20, 30, and 40 A/dm^2. For the PT implants, mainly the rutile TiO_2 phase was observed, while anatase was exclusively observed for 5 min of oxidation time. Both after 5 and 10 min of PEO processing, the $Ca_{10}(PO_4)_6(OH)_2$ (hydroxyapatite) phase as well as $CaTiO_3$ and $Ca_3(PO_4)_2$ were present. $CaTiO_3$ and hydroxyapatite were not detected on the PT–Sr implants, while $Ca_4H_2(P_3O_{10})_2$ and $Sr_8Ca_{2.5}(PO_4)_7$ phases were detected exclusively on the PT–Sr implants after 10 min of oxidation with current densities of 30 and 40 A/dm^2. Furthermore, $SrTiO_3$ and $Sr_{10}(PO_4)_6(OH)_2$ were detected on all the PT–Sr implants, with $Sr_{10}(PO_4)_6(OH)_2$ being observed more frequently with current densities of 30 and 40 A/dm^2. On the PT–Sr implants, primarily the phases pertaining to the base metal were observed with scarce rutile phases for current densities of 30 and 40 A/dm^2. After 10 min of PEO processing with current densities of 30 and 40 A/dm^2 anatase was detected.

3.6. Bioactivity of biofunctionalized implants

In general, the surface of the PT–Sr implants resembled the surface of the PT implants oxidized for 5 min at 20 A/dm^2. Therefore, the metabolic activity of MC3T3-E1 cells cultured on the implants in standard and osteogenic media was determined using a Presto Blue assay on NT, PT implants biofunctionalized for 5 min at 20 A/dm^2 and all PT–Sr implants. With the osteogenic medium and after 3 days of culture (Fig. 5A) the metabolic activity differed significantly between the NT and PT ($p < 0.05$) and PT–Sr 20 A/dm^2 implants for 10 min ($p < 0.001$), PT and PT–Sr 30 A/dm^2 for 10 min ($p < 0.001$) and PT–Sr 40 A/dm^2 for 10 min ($p < 0.001$). After 7 days of culture, significant differences were observed between the NT and PT–Sr 30 A/dm^2 for 10 min ($p < 0.05$) and PT–Sr 40 A/dm^2 for 10 min ($p < 0.001$) as well as between PT–Sr 20 A/dm^2 and PT–Sr 40 A/dm^2 for 10 min ($p < 0.01$). After 14 days, there was a significant difference between NT and PT–Sr 40 A/dm^2 for 10 min ($p < 0.05$). Without the osteogenic medium and after 3 days of cell culture, the metabolic activity differed significantly (Fig. 5B) between NT and PT–Sr 20 A/dm^2 for 10 min ($p < 0.05$), PT and PT–Sr 30 A/dm^2 for 5 min ($p < 0.05$), PT and PT–Sr 30 A/dm^2 for 10 min ($p < 0.05$) and PT–Sr 20 A/dm^2 and PT–Sr 30 A/dm^2 for 10 min ($p < 0.05$). After 7 days, there were significant differences between PT–Sr 20 A/dm^2 and PT–Sr 40 A/dm^2 for 10 min ($p < 0.05$) as well as PT–Sr 40 A/dm^2 for 5 and 10 min ($p < 0.05$). Comparing the metabolic activity in the presence of or without osteogenic medium, the results did not differ significantly.

The levels of ALP activity in osteogenic medium (Fig. 5C), differed significantly after 14 days between NT and PT–Sr 20 A/dm^2 for 5 min ($p < 0.05$), PT–Sr 20 A/dm^2 for 10 min ($p < 0.001$) and PT–Sr 40 A/dm^2 for 5 min ($p < 0.05$). Without the osteogenic medium (Fig. 5D), there were significant differences in the ALP activity after 11 days between PT–Sr 20 A/dm^2 and PT–Sr 40 A/dm^2 for 10 min ($p < 0.01$). After 14 days, there was only a significant difference between PT and PT–Sr 40 A/dm^2 for 10 min ($p < 0.01$). Without the osteogenic medium, the levels of the ALP activity were on average 4-fold lower than in the presence of the osteogenic medium. SEM analysis of the cultured cells on the implant surface for 7 days demonstrated a wide coverage of the surface by the MC3T3-E1 cells under all conditions (Fig. 5E).

4. Discussion

Given the enhanced need for orthopedic implants, the surface biofunctionalization of AM porous titanium implants has gained significant momentum. However, the biofunctionalization of porous structures remains challenging. While PEO has been successfully applied to create bioactive surfaces with osteogenic and antibacterial behavior on highly porous AM titanium implants [14,38], there is limited understanding of the contribution of individual PEO processing parameters to the generation of bioactivity on titanium biomaterials. Therefore, the possibilities to maximize the bioactivity of titanium implants by this versatile process are not fully explored and harnessed.

During PEO processing, ionic species present in the PEO electrolyte can become part of the titanium oxide layer. The composition of the electrolyte, therefore, directly governs the bioactivity of the biofunctionalized implant surfaces. In this study, we used Ca/P-based PEO electrolytes as they have been shown to generate osteogenic surfaces, partly due to hydroxyapatite formation during the PEO process [14]. In addition, strontium was added as this has been shown to further enhance the osteogenic capacity [33,39] and, more recently, to possibly boost the antibacterial potential of AgNPs incorporated in such layers [38]. To incorporate different levels of Sr, various current densities (namely 20, 30 and 40 A/dm^2) and oxidation time (namely 5 and 10 min) were used. Altering the PEO electrolyte affects the PEO process, which in turn changes the surface morphology [20]. The SEM analysis of the surface of the PT–Sr implants revealed a porous surface with smaller pores as compared to the PT implants. An oxidation time of 10 min with current densities of 30 and 40 A/dm^2 resulted in reduced porosity due to a partial destruction of the top surface layer. The smaller pore size of the PT-Sr implants may be associated with the lower voltage stems from a higher electrolyte conductivity for the PT–Sr electrolytes compared to the PT electrolytes.

Both enhancing the current density and oxidation time affected the surface morphology of the PT implants, as the pore density was reduced

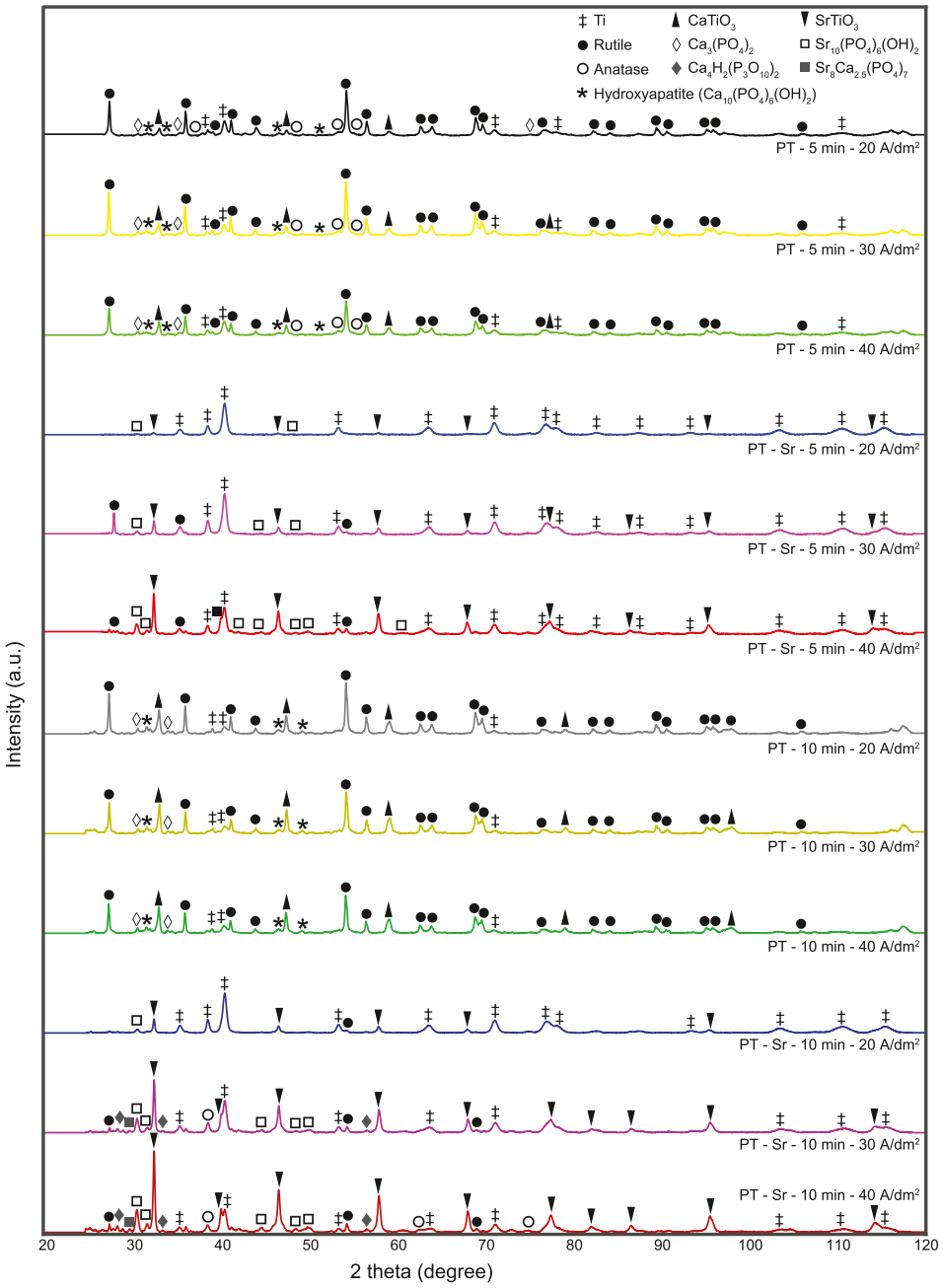

Fig. 4. The X-ray diffraction spectra of the implants after PEO biofunctionalization.

while the pore size increased. This continued until 10 min oxidation with 40 A/dm^2 which resulted in destruction of the oxide layer and subsequent reduction of pore sizes. The changes were more pronounced for longer oxidation times, which is in line with the findings of other studies [40,41]. This increased pore diameter is caused by the rising spark size and intensity and the accompanying buildup of pressures, causing an expansion in the pore diameter and making pores increasingly interconnected [42]. However, the surface morphology of the PT–Sr implants was barely affected by the current density or oxidation time, due to the small and less intense spark discharges caused by the presence of strontium to the PEO electrolyte. Notably, the surface morphology of the PT-Sr implants resembled the morphology of the PT implants oxidized at the lowest current density and shortest time (*i.e.*, 20 A/dm^2 and 5 min).

Since the current density and oxidation time alter the growth of the TiO_2 layer during PEO processing, we also explored the thickness and cross-section morphology of the TiO_2 surface layer. For all experimental groups, three different sections were observed in the TiO_2 layer: a thin, fully dense, and continuous barrier layer at the interface between oxide layer and implant substrate, followed by a layer with large pores, and on top a denser outer layer. This layer build-up is the result of different phases during the PEO process. The barrier layer is formed before dielectric breakdown by the inwards migration of the O^{2-} and the migration of titanium ions outwards [43]. After dielectric breakdown, the continuous build up and destruction of the layer occurs, leading to the outwards expansion of the oxide layer and intensified spark discharging resulting in the formation of larger, protruding pores that are increasingly interconnected [12]. The oxide layer was thinner for all the PT–Sr implants as compared to the PT implants. In addition, the pore size of the PT–Sr implants was smaller, reflecting the surface pore analysis. The thickness of the oxide layer was enhanced to a large extent by extending the oxidation time and to smaller extents by increasing the

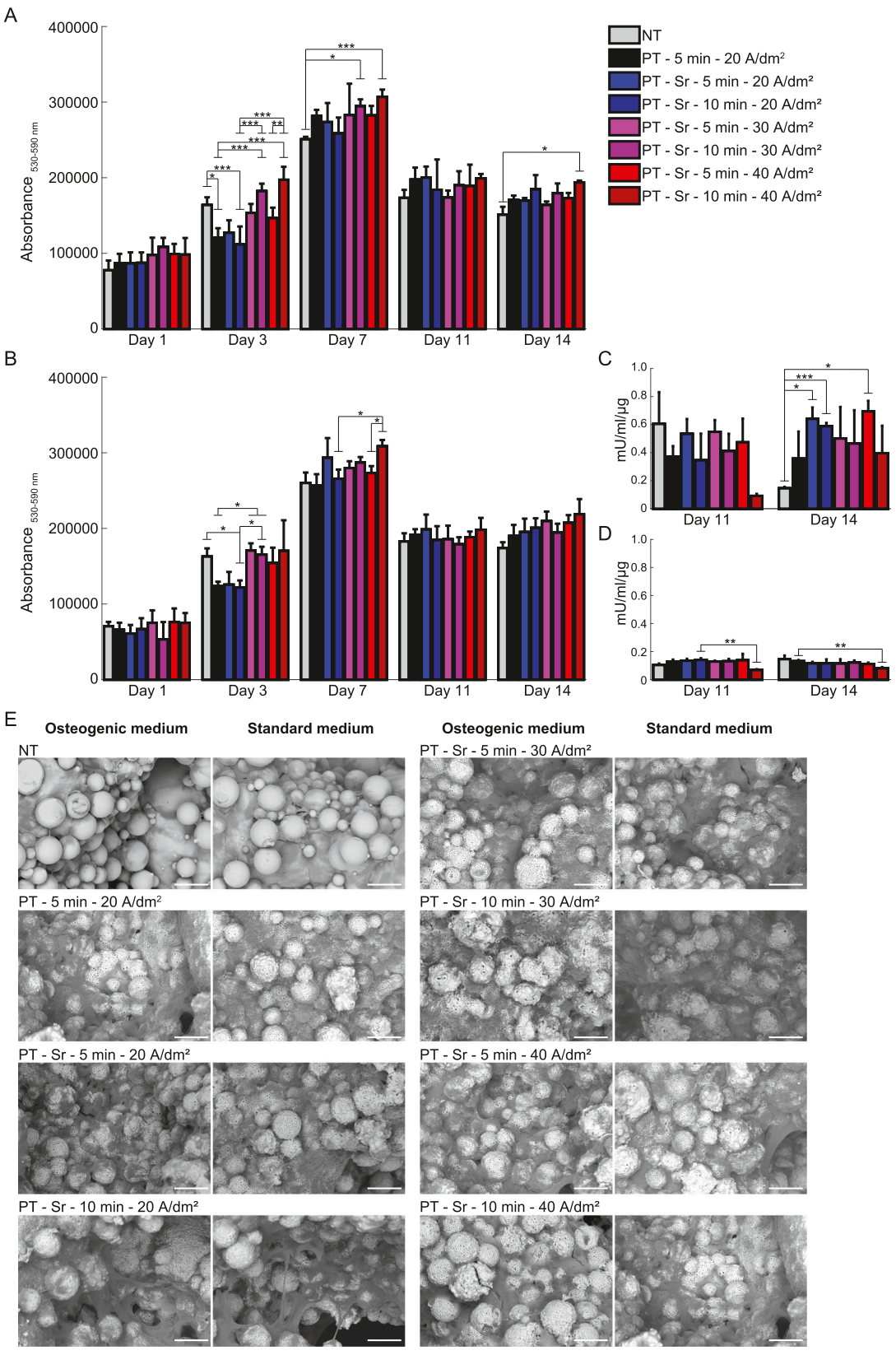

Fig. 5. The osteogenic capacity of the MC3T3-E1 cells cultured on the implant surfaces ($n = 4$). Determination of the metabolic activity by the Presto Blue assay of MC3T3-E1 cells cultured on the implants after 1, 3, 7, 11, and 14 days of culture (A) with and (B) without the addition of the osteogenic differentiation medium after 2 days. The measurement of the ALP activity after 11 and 14 days (C) with and (D) without the addition of the osteogenic differentiation medium. (E) The SEM images of the cells on the implants after 7 days of culture in osteogenic and standard culture medium. * $p < 0.05$, ** $p < 0.01$, *** $p < 0.001$. Scale bar = 50 µm.

current density, which is in line with the results of previous studies [44].

An analysis of the ion release kinetics indicated that both the oxidation time and current density enhanced the release of the Ca and Sr ions, which correlated with the enhanced thickness of the oxide layer that functions as a reservoir for ions to be released. Due to increased current densities and prolonged oxidation times, the electrical field between anode and cathode is increased, thereby enhancing the migration of the Ca and Sr ions into the growing oxide layer [45]. The release of Ca was reduced for the PT–Sr implants in comparison with the PT implants, reflecting the observation that Ca is largely replaced by strontium in the case of PT–Sr implants, as confirmed by EDS analysis. This phenomenon has also been observed in other studies [46]. For all the PT–Sr implants, except for 5 min of oxidation with a current density of 20 A/dm^2, the release rate of Sr^{2+} was higher than that of Ca^{2+}.

During PEO processing, spark discharges may lead to local temperatures of up to 3500 K [47], resulting in the mixing of the species that originate from the substrate and those present in the electrolyte. Nanocrystalline phases are formed due to the increasing temperatures and their formation increases with the applied energy input [48]. Initially, anatase is formed during the PEO process, followed by increased rutile formation over time due to more intense spark discharges with concurring rise in local temperature and pressure [49]. These nanocrystalline phases are known to induce photocatalytic activity and contribute to antibacterial activity [50]. In this study, we observed that enhanced oxidation time and current densities induced numerous phase changes. The composition of the electrolyte affects the crystallinity of the TiO_2 layer due to altered spark discharge formation and the incorporation of the species present in the PEO electrolyte [51]. We observed that the PT–Sr implants demonstrated more intense Ti peaks from the substrate, indicating a thinner oxide layer in comparison with the PT implants. Furthermore, less rutile was observed in comparison with the PT implants. This is due to a less intense spark discharging and concurring lower temperatures during the PEO process.

The formation of both rutile and anatase phases has been shown to stimulate the formation of hydroxyapatite and other Ca/P phases on titanium surfaces [52]. Furthermore, the photocatalytic activity of anatase and rutile increases with the hydroxyl density at the implant surface during spark discharging [53,54]. As a result, Ti-OH is formed that, together with Ca^{2+} and PO_4^{3-} delivered by the electrolyte, induce the nucleation and formation of hydroxyapatite crystals [55,56]. We observed higher numbers of crystalline Ca/P and strontium-Ca/P phases on the implant surfaces which were treated for longer oxidation times and also displayed higher levels of rutile and anatase. Interestingly, we observed hydroxyapatite on the PT implants, but not on the PT–Sr implants. Therefore, altering the oxidation time and composition of the PEO electrolyte directly affected the formation of crystalline TiO_2 and Ca/P phases on the implant surface. In previous work [14], we have observed that the growth rate observed during the PEO process is not affected by the different microstructure of additively manufactured implants in comparison with that of solid implants made from annealed Ti6Al4V. However, the complex micro-architecture of selective laser melted implants is likely to affect the internal fluid flow, resulting in altered local cooling of the electrolyte and potentially increased temperature during plasma discharging. These local increases of temperature in turn could contribute to the formation of hydroxyapatite phases.

Surface biofunctionalization by PEO has been shown to improve cellular behavior including cell adhesion, osteogenic differentiation, and matrix mineralization, which is generally attributed to the microporous surface morphology [57,58] and the presence of Ca/P as well as strontium on the implant surface [59–61]. Moreover, the presence of hydroxyapatite has been shown to enhance the osseointegration of titanium implants [62–64]. We, therefore, investigated whether the observed changes in the implant surface morphology and phase composition due to the addition of strontium to the PEO electrolyte as well as the variation of the current density and oxidation time affected the osteogenic behavior of preosteoblast MC3T3-E1 cells cultured on the implant surfaces.

We performed those experiments both in standard culture medium and in an osteogenic medium. The metabolic activity was analyzed up to 14 days and was not significantly different between the specimens cultured in standard and osteogenic medium. Moreover, after 7 days, the metabolic activity decreased for all surfaces and culture conditions and this is likely caused by a stop in cell proliferation as the implant surface was increasingly covered. The osteogenic medium enhanced the ALP activity, which is a differentiation marker, of the MC3T3-E1 cells on any implant at each time point as compared to the specimens cultured in the standard medium. After 14 days, the ALP activity of the PT–Sr implants biofunctionalized with a current density of 20 A/dm^2 for both 5 and 10 min as well as a current density of 40 A/dm^2 for 5 min was enhanced in comparison with the NT implants. The trend also indicates higher average ALP activities of these PT–Sr implants relative to the PT implants oxidized at 20 for 5 min, although not statistically significant. These PT–Sr implants had a surface morphology comparable with the PT implants oxidized at 20 A/dm^2 for 5 min and released the lower amounts of Sr ions compared to the other PT–Sr implants.

Our results suggest that the osteogenic behavior of the implants may be determined by a combination of surface morphology and Sr ion release, since an unfavorable surface morphology and too high doses of strontium may hamper the osteogenic differentiation of cells and induce apoptosis [65–67]. Surface characteristics including porosity [57], pore size [68], pore shape [69], and the presence of TiO_2 [70] and Ca/P/Sr-based phases [21,33,60] all have been shown to affect osteogenesis. On the macroscale, a lower porosity has been shown to enhance osteogenic differentiation *in vitro*, while a higher porosity and larger pore size has been found to result in greater bone ingrowth *in vivo* due to enhanced vascularization [68]. The PEO-biofunctionalized implants with increased microporosity have exhibited enhanced peri-implant bone formation *in vivo* [57]. Furthermore, both hydroxyapatite- and strontium hydroxyapatite-containing PEO-biofunctionalized implants are found to stimulate osteogenic differentiation *in vitro* and result in a higher bonding strength *in vivo* [33]. Finally, previous studies have reported an association between an increased microporosity and enhanced cell adhesion, cell proliferation, and ALP activity *in vitro* [59]. To fully pinpoint the contribution of each individual surface characteristic in our study, an extensive investigation of each separate characteristic needs to be performed, which is suggested for future studies.

In this study PEO processing was performed in AC mode, however also other PEO processing parameters can be explored, including the use of DC mode, pulsed uni- or bipolar current, different frequencies and varying duty cycles. The use of DC mode may result in difficulties to control the surface discharge kinetics [18]. Therefore, unipolar or bipolar pulse current regimes are used to control the spark duration [71]. Thereby the heat conditions during PEO are regulated and as such the surface morphology and chemical composition. Surfaces produced in pulsed bipolar mode possess a higher porosity due to enhanced spark discharges compared to unipolar mode [72]. In addition, with pulsed bipolar mode a larger proportion of the oxidized implant surface was composed of elements from the PEO electrolyte, rather than from the implant substrate [73]. However, when the cathode pulse was increased over a certain optimum the thickness of the titanium oxide layer was decreased [74].

The properties of the surfaces can be influenced by the duty cycles of the unipolar and bipolar pulsed modes, *i.e.* varying the time of current during each period. In this way the power of the plasma discharge can be enhanced by shorter pulse durations and increased voltages or currents [75]. As a result enhanced duty cycles will lead to increased heat generation and spark energy, thereby generating larger pores [76]. In addition, the frequency of the pulses can be changed, with higher frequencies leading to enhanced porosity and corrosion resistance [77]. Furthermore, the fraction of anatase and rutile phases can be affected by varying the frequencies [78]. Moreover, long duty cycles combined with high frequencies have shown to support the apatite forming capacity of

the implant surfaces [79]. However, the effects of these PEO processing parameters on the osteogenic capacity of the implant surface remain to be elucidated.

Further exploration of the effects of the concentration of strontium in the PEO electrolyte and the electrical parameters is needed to fully optimize the ratio of strontium and Ca release on an implant with osteogenic surface morphology. Combined with antibacterial agents [7,14], such as antibiotics or inorganic nanoparticles, this will generate potent multifunctional surfaces on future AM porous titanium implants. The next evaluation steps should include *in vivo* experiments.

5. Conclusions

In this study, we investigated the effects of the composition of calcium and strontium-based electrolytes, current density, and oxidation time on the surface morphology, phase formation, ion release, metabolic activity, and osteogenic properties of AM porous titanium implants. The implants biofunctionalized with strontium displayed smaller pore sizes, a thinner TiO_2 layer thickness, four-fold lower rate of Ca^{2+} release, predominantly anatase TiO_2 phases and Sr-containing phases as compared to the implants biofunctionalized in electrolytes containing only Ca/P species. Increasing the oxidation time resulted in a rougher surface with bigger pores, up to 4.4 fold thickening of the TiO_2 surface layer, and enhanced formation of Ca/P and TiO_2 phases to a further extent than increasing the current density. The rate of the Ca^{2+} release was enhanced by up to 1.3 and 1.2 folds and that of the Sr^{2+} release by up to 3.5 and 2.7 folds when the higher values of the current density and oxidation time were used, respectively. The different current densities and oxidation times resulted in varying metabolic activities after 3 and 7 days of the culture of MC3T3-E1 cells while the ALP activity was enhanced after 14 days for PEO biofunctionalization in Sr-containing electrolytes with a current density of 20 A/dm^2 for both 5 and 10 min, as well as with a current density of 40 A/dm^2 for 5 min. Altogether, changing the oxidation time and current density caused significant changes in the surface morphology, Sr incorporation and bioactivity of AM porous titanium implants.

CRediT authorship contribution statement

I.A.J. van Hengel: Conceptualization, Investigation, Methodology, Writing – original draft, Writing – review & editing, Visualization, Supervision. **M. Laçin:** Investigation, Methodology, Writing – original draft. **M. Minneboo:** Investigation, Methodology. **L.E. Fratila-Apachitei:** Conceptualization, Methodology, Resources, Writing – review & editing, Supervision. **I. Apachitei:** Conceptualization, Methodology, Resources, Writing – review & editing, Supervision. **A.A. Zadpoor:** Conceptualization, Resources, Writing – review & editing, Supervision, Funding acquisition.

Declaration of competing interest

The authors declare that they have no known competing financial interests or personal relationships that could have appeared to influence the work reported in this paper.

Acknowledgements

The research for this paper was financially supported by the Prosperos project, funded by the Interreg VA Flanders – The Netherlands program, CCI grant no. 2014TC16RFCB046.

References

[1] H. Maradit Kremers, D.R. Larson, C.S. Crowson, W.K. Kremers, R.E. Washington, C. A. Steiner, W.A. Jiranek, D.J. Berry, Prevalence of total hip and knee replacement in the United States, J. Bone Joint Surg. Am. 97 (2015) 1386–97.
[2] K. Willemsen, R. Nizak, H.J. Noordmans, R.M. Castelein, H. Weinans, M.C. Kruyt, Challenges in the design and regulatory approval of 3D-printed surgical implants: a two-case series, The Lancet Digital Health 1 (2019) e163–e171.
[3] E.D. Sheha, S.D. Gandhi, M.W. Colman, 3D printing in spine surgery, Ann Transl Med 7 (2019) S164.
[4] K.C. Wong, 3D-printed patient-specific applications in orthopedics, Orthop. Res. Rev. 8 (2016) 57–66.
[5] H.M.A. Kolken, S. Janbaz, S.M.A. Leeflang, K. Lietaert, H.H. Weinans, A. A. Zadpoor, Rationally designed meta-implants: a combination of auxetic and conventional meta-biomaterials, Materials Horizons 5 (2018) 28–35.
[6] A.A. Zadpoor, Additively manufactured porous metallic biomaterials, J. Mater. Chem. B 7 (2019) 4088–4117.
[7] S. Bakhshandeh, Z. Gorgin Karaji, K. Lietaert, A.C. Fluit, C.H.E. Boel, H.C. Vogely, T. Vermonden, W.E. Hennink, H. Weinans, A.A. Zadpoor, S. Amin Yavari, Simultaneous delivery of multiple antibacterial agents from additively manufactured porous biomaterials to fully eradicate planktonic and adherent Staphylococcus aureus, ACS Appl. Mater. Interfaces 9 (2017) 25691–25699.
[8] L. Lara Rodriguez, P.A. Sundaram, E. Rosim-Fachini, A.M. Padovani, N. Diffoot-Carlo, Plasma electrolytic oxidation coatings on gammaTiAl alloy for potential biomedical applications, J Biomed Mater Res B Appl Biomater 102 (2014) 988–1001.
[9] B.S. Necula, I. Apachitei, L.E. Fratila-Apachitei, E.J. van Langelaan, J. Duszczyk, Titanium bone implants with superimposed micro/nano-scale porosity and antibacterial capability, Appl. Surf. Sci. 273 (2013) 310–314.
[10] S.A. Yavari, B.S. Necula, L.E. Fratila-Apachitei, J. Duszczyk, I. Apachitei, Biofunctional surfaces by plasma electrolytic oxidation on titanium biomedical alloys, Surf. Eng. 32 (2016) 411–417.
[11] T.W. Clyne, S.C. Troughton, A review of recent work on discharge characteristics during plasma electrolytic oxidation of various metals, Int. Mater. Rev. 64 (2018) 127–162.
[12] B.S. Necula, I. Apachitei, F.D. Tichelaar, L.E. Fratila-Apachitei, J. Duszczyk, An electron microscopical study on the growth of TiO2-Ag antibacterial coatings on Ti6Al7Nb biomedical alloy, Acta Biomater. 7 (2011) 2751–7.
[13] E. Matykina, P. Skeldon, G.E. Thompson, Fundamental and practical evaluations of PEO coatings of titanium, International Heat Treatment and Surface Engineering 3 (1–2) (2013) 45–51.
[14] I.A.J. van Hengel, M. Riool, L.E. Fratila-Apachitei, J. Witte-Bouma, E. Farrell, A. A. Zadpoor, S.A.J. Zaat, I. Apachitei, Selective laser melting porous metallic implants with immobilized silver nanoparticles kill and prevent biofilm formation by methicillin-resistant Staphylococcus aureus, Biomaterials 140 (2017) 1–15.
[15] Z. Gorgin Karaji, R. Hedayati, B. Pouran, I. Apachitei, A.A. Zadpoor, Effects of plasma electrolytic oxidation process on the mechanical properties of additively manufactured porous biomaterials, Mater. Sci. Eng. C Mater. Biol. Appl. 76 (2017) 406–416.
[16] S. Aliasghari, A. Němcová, P. Skeldon, G.E. Thompson, Influence of coating morphology on adhesive bonding of titanium pre-treated by plasma electrolytic oxidation, Surf. Coat. Technol. 289 (2016) 101–109.
[17] H. Sharifi, M. Aliofkhazraei, G.B. Darband, S. Shrestha, A review on adhesion strength of Peo coatings by scratch test method, Surf. Rev. Lett. 25 (03) (2018).
[18] A.L. Yerokhin, X. Nie, A. Leyland, A. Matthews, S.J. Dowey, Plasma electrolysis for surface engineering, Surf. Coat. Technol. 122 (1999) 73–93.
[19] Y. Wang, T. Lei, B. Jiang, L. Guo, Growth, microstructure and mechanical properties of microarc oxidation coatings on titanium alloy in phosphate-containing solution, Appl. Surf. Sci. 233 (2004) 258–267.
[20] E. Ahounbar, S.M. Mousavi Khoei, H. Omidvar, Characteristics of in-situ synthesized hydroxyapatite on TiO2 ceramic via plasma electrolytic oxidation, Ceram. Int. 45 (2019) 3118–3125.
[21] Y.W. Lim, S.Y. Kwon, D.H. Sun, H.E. Kim, Y.S. Kim, Enhanced cell integration to titanium alloy by surface treatment with microarc oxidation: a pilot study, Clin. Orthop. Relat. Res. 467 (2009) 2251–8.
[22] S. Marques Ida, N.C. da Cruz, R. Landers, J.C. Yuan, M.F. Mesquita, C. Sukotjo, M. T. Mathew, V.A. Barao, Incorporation of Ca, P, and Si on bioactive coatings produced by plasma electrolytic oxidation: the role of electrolyte concentration and treatment duration, Biointerphases 10 (2015), 041002.
[23] X. Lu, M. Mohedano, C. Blawert, E. Matykina, R. Arrabal, K.U. Kainer, M. L. Zheludkevich, Plasma electrolytic oxidation coatings with particle additions – a review, Surf. Coat. Technol. 307 (2016) 1165–1182.
[24] I.A.J. van Hengel, N.E. Putra, M. Tierolf, M. Minneboo, A.C. Fluit, L.E. Fratila-Apachitei, I. Apachitei, A.A. Zadpoor, Biofunctionalization of selective laser melted porous titanium using silver and zinc nanoparticles to prevent infections by antibiotic-resistant bacteria, Acta Biomater. 107 (2020) 325–337.
[25] L. Cianferotti, F. D'Asta, M.L. Brandi, A review on strontium ranelate long-term antifracture efficacy in the treatment of postmenopausal osteoporosis, Ther Adv Musculoskelet Dis 5(3) (2013) 127–39.
[26] J.Y. Reginster, J.M. Kaufman, S. Goemaere, J.P. Devogelaer, C.L. Benhamou, D. Felsenberg, M. Diaz-Curiel, M.L. Brandi, J. Badurski, J. Wark, A. Balogh, O. Bruyere, C. Roux, Maintenance of antifracture efficacy over 10 years with strontium ranelate in postmenopausal osteoporosis, Osteoporos. Int. 23(3) (2012) 1115–22.
[27] J.Y. Reginster, Cardiac concerns associated with strontium ranelate, Expert Opin. Drug Saf. 13(9) (2014) 1209–13.
[28] L. Kyllonen, M. D'Este, M. Alini, D. Eglin, Local drug delivery for enhancing fracture healing in osteoporotic bone, Acta Biomater. 11 (2015) 412–34.
[29] E. Gentleman, Y.C. Fredholm, G. Jell, N. Lotfibakhshaiesh, M.D. O'Donnell, R.G. Hill, M.M. Stevens, The effects of strontium-substituted bioactive glasses on osteoblasts and osteoclasts in vitro, Biomaterials 31(14) (2010) 3949–56.

[30] M. Yamaguchi, M.N. Weitzmann, The intact strontium ranelate complex stimulates osteoblastogenesis and suppresses osteoclastogenesis by antagonizing NF-kappaB activation, Mol. Cell. Biochem. 359(1–2) (2012) 399–407.

[31] Y. Dang, L. Zhang, W. Song, B. Chang, T. Han, Y. Zhang, L. Zhao, In vivo osseointegration of Ti implants with a strontium-containing nanotubular coating, Int. J. Nanomedicine 11 (2016) 1003–11.

[32] A. Henriques Lourenco, N. Neves, C. Ribeiro-Machado, S.R. Sousa, M. Lamghari, C. C. Barrias, A. Trigo Cabral, M.A. Barbosa, C.C. Ribeiro, Injectable hybrid system for strontium local delivery promotes bone regeneration in a rat critical-sized defect model, Sci. Rep. 7 (1) (2017) 5098.

[33] C.J. Chung, R.T. Su, H.J. Chu, H.T. Chen, H.K. Tsou, J.L. He, Plasma electrolytic oxidation of titanium and improvement in osseointegration, J Biomed Mater Res B Appl Biomater 101 (2013) 1023–30.

[34] J.-M. Yu, H.-C. Choe, Morphology changes and bone formation on PEO-treated Ti-6Al-4V alloy in electrolyte containing Ca, P, Sr, and Si ions, Appl. Surf. Sci. 477 (2019) 121–130.

[35] I.A.J. van Hengel, F.S.A. Gelderman, S. Athanasiadis, M. Minneboo, H. Weinans, A. C. Fluit, B.C.J. van der Eerden, L.E. Fratila-Apachitei, I. Apachitei, A.A. Zadpoor, Functionality-packed additively manufactured porous titanium implants, Materials Today Bio 7 (2020).

[36] M. Montazeri, C. Dehghanian, M. Shokouhfar, A. Baradaran, Investigation of the voltage and time effects on the formation of hydroxyapatite-containing titania prepared by plasma electrolytic oxidation on Ti–6Al–4V alloy and its corrosion behavior, Appl. Surf. Sci. 257 (2011) 7268–7275.

[37] A. Kossenko, S. Lugovskoy, N. Astashina, A. Lugovskoy, M. Zinigrad, Effect of time on the formation of hydroxyapatite in PEO process with hydrothermal treatment of the Ti-6Al-4V alloy, Glas. Phys. Chem. 39 (2013) 639–642.

[38] I.A.J. van Hengel, M. Tierolf, V.P.M. Valerio, M. Minneboo, A.C. Fluit, L.E. Fratila-Apachitei, I. Apachitei, A.A. Zadpoor, Self-defending additively manufactured bone implants bearing silver and copper nanoparticles, J. Mater. Chem. B 8 (2020) 1589–1602.

[39] H.-P. Teng, H.-Y. Lin, Y.-H. Huang, F.-H. Lu, Formation of strontium-substituted hydroxyapatite coatings on bulk Ti and TiN-coated substrates by plasma electrolytic oxidation, Surf. Coat. Technol. 350 (2018) 1112–1119.

[40] M. Shokouhfar, C. Dehghanian, M. Montazeri, A. Baradaran, Preparation of ceramic coating on Ti substrate by plasma electrolytic oxidation in different electrolytes and evaluation of its corrosion resistance: part II, Appl. Surf. Sci. 258 (7) (2012) 2416–2423.

[41] X. Zhang, Z. Yao, Z. Jiang, Y. Zhang, X. Liu, Investigation of the plasma electrolytic oxidation of Ti6Al4V under single-pulse power supply, Corros. Sci. 53 (6) (2011) 2253–2262.

[42] S. Durdu, S. Bayramoğlu, A. Demirtaş, M. Usta, A.H. Üçışık, Characterization of AZ31 mg alloy coated by plasma electrolytic oxidation, Vacuum 88 (2013) 130–133.

[43] H. Habazaki, M. Uozumi, H. Konno, K. Shimizu, P. Skeldon, G.E. Thompson, Crystallization of anodic titania on titanium and its alloys, Corros. Sci. 45 (9) (2003) 2063–2073.

[44] E. Erfanifar, M. Aliofkhazraei, H.F. Nabavi, A.S. Rouhaghdam, Growth kinetics and morphology of microarc oxidation coating on titanium, Surf. Coat. Technol. 315 (2017) 567–576.

[45] H. Hu, X. Liu, F. Meng, C. Ding, Formation and bioactivity of porous and nanostructured TiO2/beta-TCP coating on titanium, J. Nanosci. Nanotechnol. 11 (12) (2011) 10913–6.

[46] C.J. Chung, H.Y. Long, Systematic strontium substitution in hydroxyapatite coatings on titanium via micro-arc treatment and their osteoblast/osteoclast responses, Acta Biomater. 7 (2011) 4081–7.

[47] C.S. Dunleavy, I.O. Golosnoy, J.A. Curran, T.W. Clyne, Characterisation of discharge events during plasma electrolytic oxidation, Surf. Coat. Technol. 203 (22) (2009) 3410–3419.

[48] X. Liu, P.K. Chu, C. Ding, Surface nano-functionalization of biomaterials, Materials Science and Engineering: R: Reports 70(3–6) (2010) 275–302.

[49] Y. Mizukoshi, N. Masahashi, Photocatalytic activities and crystal structures of titanium dioxide by anodization: their dependence upon current density, Mater. Trans. 51 (8) (2010) 1443–1448.

[50] M. Lilja, K. Welch, M. Astrand, H. Engqvist, M. Stromme, Effect of deposition parameters on the photocatalytic activity and bioactivity of TiO2 thin films deposited by vacuum arc on Ti-6Al-4V substrates, J Biomed Mater Res B Appl Biomater 100(4) (2012) 1078–85.

[51] Z. Su, L. Zhang, F. Jiang, M. Hong, Formation of crystalline TiO2 by anodic oxidation of titanium, Progress in Natural Science: Materials International 23 (3) (2013) 294–301.

[52] M. Lilja, A. Genvad, M. Astrand, M. Stromme, H. Enqvist, Influence of microstructure and chemical composition of sputter deposited TiO2 thin films on in vitro bioactivity, J Mater Sci Mater Med 22(12) (2011) 2727–34.

[53] Y. Han, S.-H. Hong, K. Xu, Structure and in vitro bioactivity of titania-based films by micro-arc oxidation, Surf. Coat. Technol. 168(2–3) (2003) 249–258.

[54] Y. Han, K. Xu, Photoexcited formation of bone apatite-like coatings on micro-arc oxidized titanium, J. Biomed. Mater. Res. A 71(4) (2004) 608–14.

[55] T. Kokubo, H.-M. Kim, M. Kawashita, Novel bioactive materials with different mechanical properties, Biomaterials 24 (13) (2003) 2161–2175.

[56] T. Akatsu, Y. Yamada, Y. Hoshikawa, T. Onoki, Y. Shinoda, F. Wakai, Multifunctional porous titanium oxide coating with apatite forming ability and photocatalytic activity on a titanium substrate formed by plasma electrolytic oxidation, Mater. Sci. Eng. C Mater. Biol. Appl. 33(8) (2013) 4871–5.

[57] K.H. Park, S.J. Heo, J.Y. Koak, S.K. Kim, J.B. Lee, S.H. Kim, Y.J. Lim, Osseointegration of anodized titanium implants under different current voltages: a rabbit study, J. Oral Rehabil. 34 (2007) 517–27.

[58] Y. Sul, The significance of the surface properties of oxidized titanium to the bone response: special emphasis on potential biochemical bonding of oxidized titanium implant, Biomaterials 24 (22) (2003) 3893–3907.

[59] T.-E. Park, H.-C. Choe, W.A. Brantley, Bioactivity evaluation of porous TiO2 surface formed on titanium in mixed electrolyte by spark anodization, Surf. Coat. Technol. 235 (2013) 706–713.

[60] P. Whiteside, E. Matykina, J.E. Gough, P. Skeldon, G.E. Thompson, In vitro evaluation of cell proliferation and collagen synthesis on titanium following plasma electrolytic oxidation, J. Biomed. Mater. Res. A 94 (2010) 38–46.

[61] L. Zhao, Y. Wei, J. Li, Y. Han, R. Ye, Y. Zhang, Initial osteoblast functions on Ti-5Zr-3Sn-5Mo-15Nb titanium alloy surfaces modified by microarc oxidation, J. Biomed. Mater. Res. A 92(2) (2010) 432–40.

[62] H. Kusakabe, T. Sakamaki, K. Nihei, Y. Oyama, S. Yanagimoto, M. Ichimiya, J. Kimura, Y. Toyama, Osseointegration of a hydroxyapatite-coated multilayered mesh stem, Biomaterials 25(15) (2004) 2957–69.

[63] G.L. Yang, F.M. He, J.A. Hu, X.X. Wang, S.F. Zhao, Effects of biomimetically and electrochemically deposited nano-hydroxyapatite coatings on osseointegration of porous titanium implants, Oral Surg Oral Med Oral Pathol Oral Radiol Endod 107 (6) (2009) 782–9.

[64] A.E. Tami, M.M. Leitner, M.G. Baucke, T.L. Mueller, G.H. van Lenthe, R. Muller, K. Ito, Hydroxyapatite particles maintain peri-implant bone mantle during osseointegration in osteoporotic bone, Bone 45(6) (2009) 1117–24.

[65] Z. Xu, J. Long, N. Zhang, H. Cao, W. Tang, K. Shi, X. Wang, S. Moya, L. Duan, H. Pan, Y. Lai, D. Wang, G. Wang, Strong mineralization ability of strontium zinc silicate: formation of a continuous biomorphic mineralized layer with enhanced osteogenic activity, Colloids Surf B Biointerfaces 176 (2019) 420–430.

[66] A. Aimaiti, A. Maimaitiyiming, X. Boyong, K. Aji, C. Li, L. Cui, Low-dose strontium stimulates osteogenesis but high-dose doses cause apoptosis in human adipose-derived stem cells via regulation of the ERK1/2 signaling pathway, Stem Cell Res Ther 8 (1) (2017) 282.

[67] X. Guo, S. Wei, M. Lu, Z. Shao, J. Lu, L. Xia, K. Lin, D. Zou, Dose-dependent effects of strontium ranelate on ovariectomy rat bone marrow mesenchymal stem cells and human umbilical vein endothelial cells, Int. J. Biol. Sci. 12 (12) (2016) 1511–1522.

[68] V. Karageorgiou, D. Kaplan, Porosity of 3D biomaterial scaffolds and osteogenesis, Biomaterials 26 (2005) 5474–91.

[69] S. Van Bael, Y.C. Chai, S. Truscello, M. Moesen, G. Kerckhofs, H. Van Oosterwyck, J.P. Kruth, J. Schrooten, The effect of pore geometry on the in vitro biological behavior of human periosteum-derived cells seeded on selective laser-melted Ti6Al4V bone scaffolds, Acta Biomater. 8 (2012) 2824–34.

[70] X. Pan, Y. Li, A.O. Abdullah, W. Wang, M. Qi, Y. Liu, Micro/nano-hierarchical structured TiO2 coating on titanium by micro-arc oxidation enhances osteoblast adhesion and differentiation, R. Soc. Open Sci. 6 (2019), 182031.

[71] L. Casanova, L. Vicentini, M. Pedeferri, M. Ormellese, Unipolar plasma electrolytic oxidation: waveform optimisation for corrosion resistance of commercially pure titanium, Mater. Corros. 72 (2020) 1–14.

[72] R.O. Hussein, X. Nie, D.O. Northwood, A spectroscopic and microstructural study of oxide coatings produced on a Ti–6Al–4V alloy by plasma electrolytic oxidation, Mater. Chem. Phys. 134 (2012) 484–492.

[73] Z. Yao, Y. Jiang, F. Jia, Z. Jiang, F. Wang, Growth characteristics of plasma electrolytic oxidation ceramic coatings on Ti–6Al–4V alloy, Appl. Surf. Sci. 254 (2008) 4084–4091.

[74] Z. Yao, Y. Xu, Z. Jiang, F. Wang, Effects of cathode pulse at low frequency on the structure and composition of plasma electrolytic oxidation ceramic coatings, J. Alloys Compd. 488 (2009) 273–278.

[75] S.V. Gnedenkov, S.L. Sinebryukhov, A.M. Puz, A.S. Gnedenkov, I.E. Vyaliy, D. V. Mashtalyar, V. Egorkin, Plasma electrolytic oxidation coatings on titanium formed with microsecond current pulses, Solid State Phenom. 213 (2014) 149–153.

[76] I.H. Han, J.H. Choi, B.H. Zhao, H.K. Baik, I.S. Lee, Effects of electrical wave form on pore size of micro-arc oxidized TiO2 film, Key Eng. Mater. 309–311 (2006) 375–378.

[77] B.-Z. Hassan, E. Saebnoori, H. Hassannejad, A. Hassanzadeh-Tabrizi, Comparing morphology and corrosion behavior of nanostructured coatings obtained via plasma electrolytic oxidation with direct and pulse currents on commercial titanium substrate, Surf. Eng. Appl. Electrochem. 55 (2020) 667–678.

[78] H.-Y. Wang, R.-F. Zhu, Y.-P. Lu, G.-Y. Xiao, J.I.E. Ma, Y.F. Yuan, Preparation and mechanism of controllable micropores on bioceramic TiO2 coatings by plasma electrolytic oxidation, Surf. Rev. Lett. 20 (2013), 1350051.

[79] S. Gowtham, T. Arunnellaiappan, N. Rameshbabu, An investigation on pulsed DC plasma electrolytic oxidation of cp-Ti and its corrosion behaviour in simulated body fluid, Surf. Coat. Technol. 301 (2016) 63–73.